Lift Enhancement by means of Small Amplitude Airfoil Oscillations at Low Reynolds Numbers

D.J. Cleaver[1], Z. Wang[2], I. Gursul[3]
University of Bath, Bath, UK, BA2 7AY

M.R. Visbal[4]
U.S. Air Force Research Laboratory, Wright-Patterson Air Force Base, Ohio, 45433

Force and particle image velocimetry measurements were conducted on a NACA 0012 airfoil undergoing small-amplitude sinusoidal plunge oscillations at a post-stall angle of attack and Reynolds number of 10,000. With increasing frequency of oscillation, lift increases and drag decreases due to the leading-edge vortices shed and convected over the suction surface of the airfoil. Within this regime the lift coefficient increases approximately linearly with the normalized plunge velocity. Local maxima occur in the lift coefficient due to the resonance with the most unstable wake frequency, its subharmonic and first harmonic, producing the most efficient conditions for high-lift generation. At higher frequencies a second mode of flowfield occurs. The leading edge vortex remains nearer the leading-edge of the airfoil and loses its coherency through impingement with the upward moving airfoil. To capture this impingement process high-fidelity computational simulations were performed which showed the highly transitional nature of the flow and a strong interaction between the upper and lower surface vortices. A sudden loss of lift may also occur at high frequencies for larger amplitudes in this mode.

[1] Postgraduate Student, Department of Mechanical Engineering, Student Member AIAA.
[2] Lecturer, Department of Mechanical Engineering, Member AIAA.
[3] Professor, Department of Mechanical Engineering, Associate Fellow AIAA.
[4] Technical Area Leader, Computational Sciences Branch, Air Vehicles Directorate, Associate Fellow AIAA.

Nomenclature

A = peak-to-peak amplitude, $2a$

a = amplitude

c = chord

C_d = time-averaged drag coefficient, $D/0.5\rho U_\infty^2 c$

C_{d0} = drag coefficient of stationary wing

C_l = time-averaged lift coefficient, $L/0.5\rho U_\infty^2 c$

C_{l0} = lift coefficient of stationary wing

f = frequency

R = cross-correlation coefficient

Re = Reynolds number, $\rho U_\infty c/\mu$

Sr_A = Strouhal number based on amplitude, fA/U_∞

Sr_c = Strouhal number based on chord, fc/U_∞

Sr_d = Strouhal number based on frontal distance, $fc\ sin\alpha/U_\infty$

t = time, 0 is top of motion

T = plunge period

U_∞ = freestream velocity

U_{pl} = peak plunge velocity, $2\pi fa$

V = velocity magnitude

α = angle of attack

$\alpha_{eff,max}$ = maximum effective angle of attack, $\alpha + tan^{-1}(U_{pl}/U_\infty)$

$\alpha_{eff,min}$ = minimum effective angle of attack, $\alpha - tan^{-1}(U_{pl}/U_\infty)$

Γ = circulation

μ = viscosity

ρ = density

I. Introduction

Recent interest in small unmanned air vehicles (UAVs) and micro air vehicles (MAVs) has been summarized in several review articles [1,2]. As the length scale of MAVs is of the order of centimeters and they will fly at very low speeds, the Reynolds number is very low, typically Re = 10^3-10^5. At these low Reynolds numbers, separated and vortical flows are dominant, making lift and thrust generation challenging due to the strong viscous effects [3].

Due to the poor lift generation in cruise flight it will be necessary for fixed-wing MAVs to fly at relatively high angles of attack, close to the stall conditions. In addition, it will be necessary to fly in the post-stall regime during high angle of attack maneuvers and vertical gusts. Flight within these regimes may entail serious consequences. For example large-amplitude low-frequency (an order of magnitude lower than vortex shedding) flow oscillations have been experimentally observed for a low Reynolds number airfoil near stall conditions [4]. These oscillations were shown to be due to the unsteady bubble bursting resulting in periodic lift fluctuations. These low frequency flow oscillations as well as the well-known Karman vortex shedding at higher angles of attack may be harmful for MAV flight. In addition, undesired roll oscillations may develop at incidences near the stall. Large-amplitude self-excited roll oscillations have been observed for typical MAV wing planforms such as elliptical, Zimmerman, and low aspect ratio (such as AR=2) rectangular wings [5,6]. Hence the delay of stall is necessary for stable MAV flight.

Consequently active or passive flow control will be necessary to increase lift and delay stall. However at these small scales conventional flow control techniques such as blowing are not practical and often the space available is insufficient to place actuators or blowing chambers. In addition, weight, volume, and power consumption of the whole actuation system, not the actuator alone, should be addressed. For example, plasma actuators, when the whole actuation system is considered, may not be practical at these small scales. Our vision is to exploit fluid-structure interactions to control the separated flows, and thus increase lift and delay stall. To simulate these aeroelastic vibrations in this investigation we utilize forced small-amplitude oscillations. In particular, we model high aspect ratio wings with an airfoil undergoing small-amplitude plunge oscillations. In practical applications, this effect can be exploited by the torsional and bending vibrations of flexible wings and/or aeroelastic mounting of rigid wings. External excitation at resonant frequencies or self-excited wing oscillations near the stall can also be considered.

The motivation for flow control with fluid-structure interactions in the form of small-amplitude wing oscillations originates from recent studies for nonslender delta wings [7,8], which demonstrated that the flow may be reattached resulting in increased lift force in the post-stall region. More interestingly, self-excited wing vibrations of a flexible delta wing can promote reattachment of the separated shear layer and lead to impressive lift enhancement [9] in the post-stall region. The structure of the reattached flow is similar to a conical separation bubble in the time-averaged sense. For a wing with zero sweep angle and at a high angle of attack in the post-stall region, the formation of a stable separation bubble, in which the flow reattaches completely to the wing surface, is not possible. This

is owing to the lack of spanwise removal of vorticity on two-dimensional airfoils (large aspect ratio wings).

Nevertheless, partial reattachment or displacement of the separated shear layer closer to the wing surface is possible when the inherent instabilities in the separated flow are excited [10]. Depending on the wing and excitation characteristics at least three different instabilities may be important for effective excitation: (i) initial shear layer instability or its subharmonic, although this appears to be more effective for low sweep wings [7-9]; (ii) instability of the separation bubble [11]; and (iii) wake instability [12,13]. In addition, an alternative control strategy relying on much higher frequencies was discussed by Glezer et al. [14]. For small scale aircraft, small-amplitude wing oscillations could potentially excite characteristic frequencies of all three instabilities, but the much higher frequencies used by Glezer et al. [14] are not practically possible. Which instability is the best to excite will be one of the questions that we will try to answer in this paper.

We have explored the idea of using small amplitude airfoil oscillations in preliminary experiments for a NACA0012 airfoil at a post-stall incidence [15,16]. Independently, high-fidelity simulations of small-amplitude oscillations of a SD7003 airfoil at a post-stall incidence were performed [17]. These initial findings highlighted the delay of stall and lift enhancement on oscillating airfoils, and also identified an interesting phenomenon due to a strong interaction between the airfoil and vortex. In this new mode of vortex topology, a leading-edge vortex is generated during the downward motion of the airfoil and then impinges on the upward moving airfoil, resulting in rapid loss of its coherency. As a result in this flow regime no coherent vortices are convected downstream

over the suction surface of the airfoil, which has a considerable effect on the aerodynamic forces. We studied this phenomenon with further experiments and simulations for the NACA0012 airfoil. Also, the time-averaged lift force was found to have local maxima at optimal frequencies and amplitudes, and the flow physics of these observations was investigated. The purpose of this article is to summarize our findings and understanding of these phenomena. Various experimental methods including particle image velocimetry (PIV) measurements and force measurements were combined with high-fidelity simulations. The main objective is to understand the flow physics of stall delay and lift enhancement for small-amplitude airfoil oscillations.

II. Experimental Techniques

Force and PIV measurements were conducted on a plunging NACA 0012 airfoil mounted vertically in a closed-loop water tunnel. The airfoil was maintained at a fixed geometric angle of attack ($\alpha = 15°$) with the sinusoidal plunging motion acting normal to the freestream as shown in Fig. 1. Experiments were performed for Reynolds numbers Re = 10,000 and 20,000, although the vast majority of the data was obtained for Re = 10,000 only.

A. Experimental Setup

The experiments were conducted in a free-surface closed-loop water tunnel (Eidetics Model 1520) at the University of Bath. The water tunnel is capable of flow speeds in the range 0 to 0.5 m/s and has a working section of dimensions 381 mm x 508 mm x 1530

mm. The turbulence intensity has previously been measured [18] by laser Doppler velocimetry (LDV) to be less than 0.5%.

A NACA 0012 airfoil of dimensions 0.1 m chord x 0.3 m span was mounted vertically in a 'shaker' mechanism, see Fig. 2. The airfoil was constructed by rapid prototyping from SLS Duraform Prototype PA. The airfoil had two internal 8-mm diameter steel rods spanning from root to tip to ensure a high spanwise stiffness. The tip deformation was monitored with a digital camera and did not exceed 1% of the chord length for the largest amplitude and frequency. The airfoil was placed between an upper and lower end plate with clearances maintained at 2 mm. The oscillations were supplied via a Motavario 0.37 kW three-phase motor, 5:1 wormgear and IMO Jaguar Controller. The position of the root of the airfoil was measured through a rotary encoder attached to the spindle of the worm gear shaft. The rotary encoder was also used to trigger the PIV system.

Normalized amplitude of the plunge oscillations was in the range of a/c = 0.025 to 0.2. The Strouhal number based on the chord length, $Sr_c = fc/U_\infty$, of the oscillations was varied in the range of Sr_c = 0 to 3.0, with an uncertainty of ±2.3%. Uncertainties are calculated based on the methods of Moffat [19] taking into account both bias and precision errors [15].

B. Force Measurements

The forces applied in both the streamwise and cross-stream directions were measured via a two-component aluminium binocular strain gauge force balance [20]. The measured

forces include both time-dependent aerodynamic forces as well as the inertia force. However, time-averaged forces include only the time-averaged aerodynamic forces as the time-averaged inertial force is zero. No attempt was made to estimate the instantaneous aerodynamic forces, as the time-averaged aerodynamic forces are sufficient to assess the effectiveness of the airfoil oscillations.

Three force balances of varying sensitivity (hence flexibility) were used as the oscillation frequency is increased. Within their applicable ranges, the agreement between the three balances was excellent. The signal from the strain gauges was amplified by a Wheatstone bridge circuit and sampled at either 2 kHz for 20,000 samples (stationary cases), or 360 per cycle for a minimum of 50 cycles (dynamic cases). To minimize uncertainty the calibration curves consisted of twenty three points, and were performed daily before and after testing. Each data set was repeated a minimum of three times for each force balance.

The uncertainty associated with these time-averaged force measurements increases with increasing frequency. For a typical case the uncertainty of the time-averaged lift coefficient increases from ±0.03 at $Sr_c = 0$, to ±0.35 at the maximum Strouhal number. Likewise the uncertainty of the time-averaged drag coefficient increases from ±0.02 to ±0.09 within the same range.

C. PIV Measurements

A TSI 2D-PIV system consisting of dual 50 mJ Nd:YAG lasers and 8-bit CCD camera of resolution of 1600 by 1192 pixels was used to measure the velocity field in the vicinity of the airfoil. The flow was seeded with commercially available hollow glass particles with mean diameter of 4 μm. For measurements over the upper surface of the airfoil, the laser was positioned behind with the camera located under the tunnel as shown in Fig. 2(a). The shadow created by the airfoil therefore obscured the lower surface. For measurements over the lower surface the laser was positioned near the side wall of the tunnel as shown in Fig. 2(b). The PIV images were analyzed using the software Insight 3G using a recursive FFT correlator on an interrogation window size of 16 by 16 pixels to generate a vector field of 199 x 148 vectors. This gave approximately a 1.2 mm (1.2% of the chord length) spatial resolution for the upper surface, and 0.9 mm (0.9% of the chord length) for the lower surface. The estimated uncertainty for velocity measurements is 2% of the freestream velocity U_∞. The time-averaged data is derived from 500 pairs of images, the phase-averaged from 100 pairs for the upper surface, and between 100 and 250 pairs for the lower surface. Where necessary the upper and lower surface data were later merged through interpolation of the lower surface data onto the upper surface grid.

To calculate the circulation from the phase-averaged data, the vortex is located using a vortex identification algorithm [21,22] with the search centered on the point of maximum absolute vorticity. The radius of the vortex is then determined by continually expanding from the centre, one spatial resolution unit at a time, until the increase in the magnitude of circulation is negative or small (<1%). The circulation calculation itself is done using

both line integral and vorticity surface methods [23]. The agreement between the two methods was generally very good. All circulation results presented herein are derived from the average of the two.

III. Computational Approach

For these plunging airfoil simulations, the governing equations are the unfiltered full compressible Navier-Stokes equations cast in strong conservative form after introducing a general time-dependent curvilinear coordinate transformation $(x, y, z, t) \rightarrow (\xi, \eta, \zeta, \tau)$ from physical to computational space. In terms of non-dimensional variables, these equations can be written in vector notation as:

$$\frac{\partial \mathbf{Q}}{\partial \tau} + \frac{\partial \mathbf{F}_{\mathrm{I}}}{\partial \xi} + \frac{\partial \mathbf{G}_{\mathrm{I}}}{\partial \eta} + \frac{\partial \mathbf{H}_{\mathrm{I}}}{\partial \zeta} = \frac{1}{\mathrm{Re}}\left[\frac{\partial \mathbf{F}_{\mathrm{v}}}{\partial \xi} + \frac{\partial \mathbf{G}_{\mathrm{v}}}{\partial \eta} + \frac{\partial \mathbf{H}_{\mathrm{v}}}{\partial \zeta} \right] \tag{1}$$

Here $\boldsymbol{Q} = \frac{1}{\boldsymbol{J}}[\rho \quad \rho u \quad \rho v \quad \rho w \quad \rho E_t]^T$ denotes the solution vector and $\boldsymbol{J}$ is the transformation Jacobian. The inviscid and viscous fluxes can be found, for instance, in Anderson et al. [24]. In the expressions above, u, v, w are the Cartesian velocity components, ρ the density, p the pressure, and T the temperature. The perfect gas relationship $p = \rho T / (\gamma M^2)$, Sutherland's law for viscosity, and a constant molecular Prandtl numer ($Pr = 0.72$) are also assumed.

It should be noted that the above governing equations correspond to the original *unfiltered* Navier-Stokes equations, and are used without change in laminar, transitional or fully turbulent regions of the flow. Unlike the standard LES approach, no additional

sub-grid stress (SGS) and heat flux terms are appended. Instead, a high-order low-pass filter operator is applied to the conserved dependent variables during the solution of the standard Navier-Stokes equations. This highly-discriminating filter selectively damps only the evolving poorly-resolved high-frequency content of the solution. This filtering regularization procedure provides an attractive alternative to the use of standard SGS models, and has been found to yield suitable results for several canonical turbulent flows [25,26] on LES-level grids.

All simulations are performed employing the extensively validated high-order *FDL3DI* Navier-Stokes solver, described in more detail in Visbal and Gaitonde [27]. In this code, a finite-difference approach is used to discretize the governing equations, and all spatial derivatives are obtained employing a 6^{th}-order compact-differencing scheme. In order to eliminate high-frequency spurious components, an 8^{th}-order Pade-type low-pass spatial filtering operator is also incorporated [27]. This filter is applied to the conserved variables along each transformed coordinate direction after each time step or sub-iteration. For transitional and turbulent flows, this filtering technique provides an effective high-order implicit LES approach.

For the case of a maneuvering airfoil, the grid is moved in a rigid fashion using the prescribed airfoil motion. To ensure that the Geometric Conservation Law (GCL) is satisfied, the time metric terms are evaluated employing the procedures described in detail in Visbal and Gaitonde [28].

The original airfoil sharp trailing edge was rounded with a circular arc of radius $r/c \sim 0.0013$ in order to facilitate the use on an O-mesh topology. The computational mesh

consisted of *643 x 395 x 101* points in the streamwise, normal and spanwise direction, respectively. Grid points were concentrated near the airfoil in order to capture the transition process. For the three-dimensional simulations, which invoked periodicity in the spanwise direction, the mesh had a span s/c = 0.2. This value of spanwise distance was selected based on a previous study on the effect of spanwise extent for an SD7003 airfoil under similar conditions [17]. Further details on the boundary conditions can be found in [17].

Plunging simulations were started from previously computed static solutions at the corresponding mean angle of attack. Simulations were then advanced in time for more than 25 cycles in order to guarantee a time-asymptotic nearly-periodic state. A very small computational time step $\Delta t\ U_\infty / c = 4.996 \times 10^{-5}$ was prescribed in order to provide sufficient temporal resolution of the abrupt spanwise breakdown of the leading-edge vortices. This value of Δt corresponded to 6,672 time steps per cycle for a Strouhal frequency $Sr_c = 3.0$. Finally, all computations were performed employing a low freestream Mach number M_∞ = 0.05, as required with the present compressible Navier-Stokes solver.

IV. Results

This section shall initially detail the flowfields associated with small-amplitude plunge motion in both a time-averaged and phase-averaged sense. We identify two distinct modes of flowfield. Details of a strong vortex-airfoil interaction in one of these modes

are discussed and the effect this has on the time-averaged forces is analyzed. In addition, optimal frequencies for the time-averaged lift and relation to the natural instabilities are discussed in detail. Finally several other features associated with the time-averaged force coefficients are investigated.

A. Time-Averaged Flow

Fig. 3(a) presents the streamlines and the magnitude of the total velocity vector for the stationary NACA0012 airfoil at an angle of attack, $\alpha = 15^o$. There is a large region of separation over the suction surface of the airfoil. The airfoil can therefore be classified as fully stalled in agreement with force measurements presented elsewhere [29] that showed for Re = 10,000, 20,000, 30,000 and 40,000, stall occurs in the region $\alpha = 10°$ to 11°. This is consistent with previous studies [30,31] at low Reynolds numbers, Re = 4,000 – 31,000.

Fig. 3(b) demonstrates that oscillation even at small amplitude (a/c = 0.025) and low frequency (Sr_c = 0.50) significantly reduces this separated region. It is worth noting that due to the nature of time-averaged measurements the motion of the airfoil obscures a region in the direct vicinity of the airfoil. This makes the separated region appear smaller than is necessarily true. It is therefore preferable to consider the mean position of the airfoil (shown with solid line) when comparing with the stationary case. Even taking this into account the separation reduction is still significant. With increasing Strouhal number (Fig. 3(c) to 3(g)) the reduction in separation region increases so that for Sr_c = 3 the separated region is almost completely eliminated in a time-averaged sense.

A second interesting feature is the region of high velocity over the leading-edge of the airfoil. With increasing Strouhal number this region increases in size and magnitude. This region coincides with the formation and shedding of leading-edge vortices. A third feature is the region in the vicinity of the trailing-edge for Sr_c = 2.5, see Fig. 3(f). A region of low velocity is observed above the trailing-edge accompanying a region of high velocity below the trailing-edge. It will be shown later that these two features coincide with the formation of trailing-edge vortices. It will also be shown that once formed these trailing-edge vortices may form a reverse-Kármán vortex street responsible for the weak time-averaged 'jet' observed in Fig. 3(g).

At the increased amplitude of a/c = 0.050 shown in Fig. 4 there are the same three flow features (reduced separation, high velocity near the leading-edge region, and time-averaged 'jet' downstream of the trailing-edge), but with greater effect for the same Strouhal number. Indeed the reduction in separation is such that for Strouhal numbers above Sr_c = 1.5 (Fig. 4(e) to 4(g)) there is no discernible separation region. Likewise for the same Strouhal number the high velocity leading-edge region is enhanced by the greater amplitude but with the crucial difference that for $Sr_c > 2$ (Fig. 4(f) and (g)) it begins to shrink in size. It will be shown later that this reduction coincides with a new mode of leading-edge vortex behavior.

The trailing-edge flow behavior is similarly enhanced by the larger amplitude of the airfoil oscillations. For example the time-averaged jet is first apparent at Sr_c = 1.5 and grows in strength with increasing Strouhal number such that for Sr_c = 3 it contains peak time-averaged velocities of three times the freestream (as measured a half-chord

downstream of the trailing-edge). This combination of reduced time-averaged separation region, high velocity near the leading-edge, and strong time-averaged jet imply increased lift and reduced drag (or thrust production at high frequencies).

B. Phase-Averaged Flow

Now looking at the phase-averaged flowfield, Fig. 5 shows vorticity at the top (left column) and bottom (right column) of the motion for a/c = 0.050, and the same Strouhal numbers as Figures 4(c) to 4(g). For Sr_c = 1.0 (Fig. 5(a)) multiple clockwise leading-edge vortices and multiple counter-clockwise trailing-edge vortices form during the downward motion. During the upward motion these vortices gradually diffuse in a phase-averaged sense as they convect downstream. One would anticipate that during the upward motion a clockwise trailing-edge vortex should form, however for this case there is none or it is very weak. This is a result of the small plunge velocity for this case.

With the Strouhal number increased to Sr_c = 1.5 (Fig. 5(b)), the maximum and the minimum effective angles of attack are $\alpha_{eff,max} = \alpha + tan^{-1}(U_{pl}/U_\infty) = 40°$ and $\alpha_{eff,min} = \alpha - tan^{-1}(U_{pl}/U_\infty) = -10°$. As such there are now two weak clockwise vortices shed at the trailing-edge per cycle (which are visible below the trailing-edge in the left column). Furthermore the multiple counter-clockwise vortices shed from the trailing-edge have become a single, stronger vortex. In a similar manner, instead of multiple leading-edge vortices there is a single leading-edge vortex of greater maximum negative vorticity. This leading-edge vortex creates a weaker secondary vortex of opposite sign due to the vortex-boundary interaction. The creation of the large trailing-edge vortex and its interaction

with the large leading-edge vortex results in the rapid dissipation of the leading-edge vortex in the phase-averaged sense.

With the Strouhal number increased to Sr_c = 2.0 (Fig. 5(c)), the leading-edge vortex and its secondary vortex become stronger. Likewise the trailing-edge vortices have increased in strength and amalgamated so that there is now one strong counter-clockwise and one weak clockwise trailing-edge vortex shed per cycle. It is the interaction of these trailing-edge vortices with the convected leading-edge vortex that produces the interesting 'dual-branch' wake pattern. The upper branch is formed by the clockwise leading-edge vortex merging with the stronger clockwise trailing-edge vortex (just visible in left column). This merged vortex forms a dipole with the weak counter-clockwise vortex from the trailing-edge. This dipole convects downstream above the trailing-edge (clearly seen in right column). Meanwhile, the lower branch is formed by the stronger counter-clockwise trailing-edge vortex creating a dipole with the weak clockwise trailing-edge vortex. This second dipole convects downstream below the trailing-edge. The resultant dual-branch wake bears a strong resemblance to the neutral wakes of Lai and Platzer [32] that are created during the transition from drag to thrust. Indeed the corresponding time-averaged flowfield (Fig. 4(e)) shows a negligible time-averaged jet further downstream, in agreement with this description.

At Sr_c = 2.5 (Fig. 5(d)) the flowfield has changed significantly. The leading-edge vortex again forms during the downward motion but remains close to the leading-edge for a greater portion of the cycle and therefore impinges with the airfoil during the upward motion and loses its coherency. It remains nearer the leading-edge due to the

reduced wavelength of the vortices. This can be seen in the reduced vortex spacing with increasing Strouhal number shown in the right hand column of Fig. 5. The reduced wavelength is due to a combination of the decreasing period with increasing Strouhal number and the vortex convection velocity remaining approximately constant (~$0.75U_\infty$). There is one strong clockwise and one counter-clockwise trailing-edge vortex formed per cycle. As there is no interference from a convected LEV, the two TEVs combine to create a vortex dipole. The resultant reverse-Kármán vortex street is responsible for the strong time-averaged 'jet' observed in Fig. 4(f).

At Sr_c = 3.0 (Fig. 5(e)) this effect is further enhanced. In this case the leading-edge vortex is formed during the downward motion and loses its coherency entirely during the upward motion so that there is no discernible convected leading-edge vortex. As a result one observes a strong reverse-Kármán vortex street with peak phase-averaged velocities of six times the freestream. Hereafter this form of wake (no convected leading-edge vortex) shall be termed a mode-2; mode-1 refers to a leading-edge vortex which is shed and convected over the upper surface of the airfoil as in Fig. 5(c).

C. Vortex-Airfoil Interaction

It is obvious that the dramatic vortex-airfoil interaction and loss of vortex coherency will be important for the unsteady aerodynamic forces. The flow physics of this phenomenon is difficult to study experimentally as this strong interaction takes place very close to the airfoil surface for a small amplitude airfoil motion. In particular, the impingement of the vortex as the airfoil moves upward is difficult to capture with PIV

due to the airfoil's proximity. Therefore, the case shown in Fig. 5(e), a/c = 0.050 and Sr_c = 3, was simulated computationally, see Fig. 6. Shown on the left are the experimental results of the phase-averaged vorticity at four phases in the cycle, and on the right are the equivalent computational results. Also, insets show enlarged views of the flow near the leading-edge. The upper surface leading-edge vortex formation is clearly seen during the downward motion. Then during the upward motion one observes the impingement of the vortex upon the airfoil, and also the loss of coherency of the upper surface leading-edge vortex, accompanying the formation of a weaker lower surface leading-edge vortex of opposite sign. The lower surface vortex is weaker due to the asymmetry in the effective angle of attack created by the motion, i.e., $\alpha_{eff,max}$ = 58° during the downstroke versus $\alpha_{eff,min}$ = -28° during the upstroke. The experimental and computational results are generally in very good agreement in terms of size, position and strength of the vortices.

The details of the interaction during the upward motion of the airfoil are shown in terms of instantaneous vorticity fields in Figure 7. It is apparent that at all phases of the motion, and despite the low value of Reynolds number, the flow field is highly transitional and the vortices exhibit fine-scale features. At the bottom of the downstroke (Fig. 7a), the formation of the primary and secondary vortex pair above the airfoil is observed (see also its corresponding phased-averaged representation in Fig. 6c). Also noticeable are the remnants of the previous lower surface vortex which wrap around the upper surface vortex system. Examination of the three-dimensional flow field (not shown) indicates that there is significant stretching of the vortex filaments which promote further dissipation. As the airfoil moves in the upward direction, the upper surface

primary vortex moves around the leading edge due to the induced negative angle of attack and eventually impinges against the airfoil (Figs. 7c-f). The secondary vortex above the airfoil moves also around the leading edge and grows into the lower surface primary vortex. Due to the asymmetry in effective angle of attack previously noted, there is not a clearly observable lower-surface secondary vortex.

D. Vortex Modes and Drag/Thrust

This strong vortex-airfoil interaction also exists at larger amplitudes of airfoil oscillations. Figure 8 shows the phase-averaged vorticity fields for a/c = 0.100 and Sr_c = 1.75, covering both upper and lower surfaces. For this larger amplitude, this interaction and mode-2 flowfield is observed at a smaller Strouhal number compared to the small amplitude case. As the amplitude is larger, the leading-edge vortex develops further away from the airfoil surface, facilitating the use of PIV. Figures 8(a) to 8(e) show the upper surface vortex formation during the downward motion, and Figs. 8(e) to 8(a) then show its impingement during the upward motion. The main features of the interaction are similar to the earlier observations for the small-amplitude case.

In a similar manner, PIV measurements were performed [15] at regularly spaced Strouhal numbers for an amplitude range of a/c = 0.025 to 0.200 with increments of 0.025 so as to define boundaries for the two mode types in the amplitude-frequency domain space, see Fig. 9. The area to the left of the boundary therefore represents the domain of the mode-1 flowfield and the area to the right represents the domain of the

mode-2 flowfield. In the grey boundary area there is a discernible leading-edge vortex but it is weak, as in Fig. 5(d), and therefore is termed a ‘mixed’ flowfield.

As shown in Fig. 9 the Strouhal number required for the mode switch increases with decreasing amplitude. Given this trend, it would be interesting to study its dependency on normalized plunge velocity or effective angle of attack. Therefore superimposed on Fig. 9 are lines of constant maximum effective angle of attack. These lines can also be considered as lines of constant normalized plunge velocity or Strouhal number based on amplitude, $Sr_A = fA/U_\infty = f2a/U_\infty$ as:

$$\alpha_{eff,\max} = \alpha + \tan^{-1}\frac{U_{pl}}{U_\infty} = \alpha + \tan^{-1}\frac{2\pi fa}{U_\infty} = \alpha + \tan^{-1}\pi Sr_A \qquad (2)$$

Since the mode-switch band occurs in the approximate range of $\alpha_{eff,max} = 48°$ to $\alpha_{eff,max} = 68°$, or alternatively $Sr_A = 0.20$ to $Sr_A = 0.43$, one can conclude that the mode-switch does not bear a strong correlation with either constant effective angle of attack or constant Strouhal number based on amplitude. So in a similar manner to the observations of Young and Lai [33] for drag, neutral and thrust wakes, wake structure regions do not follow lines of constant Strouhal number based on amplitude.

Figure 10 presents the drag coefficient for the five amplitudes tested. It demonstrates for all amplitudes the well documented [34] reduction in drag or increase in thrust with increasing Strouhal number, with greater effect for greater amplitude. The smallest amplitude $a/c = 0.025$ did not exhibit a zero drag point because the Strouhal number range tested was insufficient. When the drag-thrust switch points are converted to Sr_A [15], the switch occurs in the range $Sr_A = 0.25$ - 0.42 with higher Sr_A for greater

amplitude. It is therefore concluded that at non-zero angles of attack Strouhal number based on amplitude is not a good measure of drag/thrust characteristics.

The drag-to-thrust switch locations are also shown in Figure 9. These points are for the four amplitudes where zero drag was observed. It is clear that a mode-2 flowfield is beneficial to thrust production. It is suggested that the mode-2 flowfield may facilitate thrust production by a stronger reverse-Kármán vortex street due to a combination of greater shedding of vorticity at the trailing-edge and no destructive interference from the convected leading-edge vortex.

E. Optimal Frequencies and Amplitudes for Time-Averaged Lift

The effect on time-averaged lift coefficient of small-amplitude oscillations is shown in Fig.11. It demonstrates that significant lift enhancement is possible with greater effect for larger amplitude. The largest time-averaged lift coefficient increase is for a/c = 0.20, C_l = 2.93, an increase of 310% over the value for a stationary airfoil, C_{l0} = 0.72, at Re = 10,000. (The value of C_{l0} is consistent with previous studies at low Reynolds numbers [30,31]).

Despite the dependency of lift coefficient on amplitude there do appear to be several peaks which are similar for all amplitudes. These can be observed at $Sr_c \approx 0.5$, around 1.1-1.2, and around 2.0-2.2. In order to eliminate any sources related to the experimental setup, the lift measurements were repeated for the same wing at a higher Reynolds number, Re = 20,000 for one amplitude (a/c = 0.2). Even though the freestream velocity was doubled, we find the same peak at Sr_c = 0.5 and virtually no effect of Reynolds

number. Having confirmed that these optimal frequencies are due to the fluid dynamics, we note that a similar peak in time-averaged lift was observed at a Strouhal number of $Sr_c \approx 0.4$ in the direct numerical simulations of Andro and Jacquin [35] for a plunging NACA 0012 airfoil at Re = 1,000. In this case the peak was attributed to an optimal interaction of the leading-edge vortices with the airfoil.

As the frequency (Strouhal number based on the chord length) or amplitude is increased, the plunge velocity (or "excitation" velocity) is also increased. Therefore, from an active flow control point of view, excitation level is not constant when either the frequency or amplitude is varied. In order to take this into account, we define a modified lift coefficient based on the vector sum of the freestream velocity and maximum plunge velocity:

$$\hat{C}_l = \frac{L}{\frac{1}{2}\rho(U_\infty^2 + U_{pl}^2)c} \tag{3}$$

Based on the data shown in Fig. 11, we present in Fig. 12 a contour plot of the modified lift coefficient normalized by the lift coefficient of the stationary airfoil, as a function of amplitude and Strouhal number based on the chord length. The most apparent feature of Fig. 12 is the existence of three regions of optimal excitation conditions with their Strouhal number ranges centered around Sr_c = 0.5, 1.0, and 2.0. It is interesting that the three regions are located on a constant plunge velocity of U_{pl}/U_∞ = 0.5 shown with a dashed line in Fig. 12. Hence, the optimum plunge velocity is approximately half the freestream velocity. The band shown with the two solid lines is the same region that separates mode-1 and mode-2 flowfields as discussed in Fig. 9. Hence, all three optimal

operating conditions have a mode-1 flowfield, confirming that convected leading-edge vortices provide the most efficient conditions for maximizing the time-averaged lift. It is also seen that loss of lift is associated with the onset of the mode-2 flowfield.

Returning to the frequency range of the optimal excitation conditions for the airfoil in post-stall (with fully separated flow at the leading-edge), Wu et al. [12] demonstrate the effectiveness of the vortex lock-in phenomenon in flow control, when the excitation frequency is equal to the natural frequency of vortex shedding in the wake and its first harmonic. They also report that subharmonic resonance with vortex shedding lead to the largest lift increase in their numerical simulations. In an experimental study, Miranda et al. [13] also confirmed the effectiveness of excitation at the subharmonic and fundamental frequency of the wake natural shedding frequency for an airfoil with a sharp leading-edge. We measured the natural shedding frequency by means of a hot-film placed in the wake of the airfoil. The signal was recorded and the frequency spectra were calculated for various locations. A typical example is shown in Fig. 13. The inset shows an instantaneous flow field measured by PIV and the location of the hot-film measurement. Measurements repeated at different locations suggest that the average of the dominant peaks is at $Sr_c = 0.89$ for a streamwise station one chord length downstream of the trailing-edge. The dominant frequency corresponds to a Strouhal number based on frontal distance $Sr_d = fc \sin\alpha / U_\infty = 0.23$, which agrees well with the previous results (in the range $Sr_d = 0.16$-0.22) for flat plates and airfoils [13, 36-38]. Hence, we suggest that the peak in lift at $Sr_c \approx 1.0$ in Fig. 12 corresponds to the natural vortex shedding

frequency in the wake. The peak at $Sr_c \approx 0.5$ would therefore be the subharmonic, and the peak at $Sr_c \approx 2.0$ the first harmonic of the natural shedding frequency.

One expects that when oscillated at the natural shedding frequency, its harmonics or subharmonics, the wake becomes more ordered and synchronized in a similar manner to vortex lock-in of oscillating cylinders [39]. This results in an increase of spanwise correlation of the flow. To confirm this, simultaneous two-point measurements of velocity with two hot-film probes were performed in the wake of the oscillating airfoil and the cross-correlation coefficient was calculated. Figure 14 shows the variation of the correlation coefficient as a function of excitation (oscillation) frequency of the airfoil (Strouhal number) for the measurement locations marked in the inset. The hot-film probes were separated by a distance of 1.3*c* about the mid-span. It is seen that there are strong peaks at $Sr_c \approx 0.45$ and $Sr_c \approx 1$, and a weaker and broader peak around $Sr_c \approx 2$. Hence we conclude that the peaks in the lift are due to the resonance with the fundamental, subharmonic and first harmonic of the natural vortex shedding in the wake.

Finally, we estimated the cycle-averaged power input during the plunge oscillation, using the methodology employed in [40]. For the case of the NACA 0012 airfoil at the mean angle of attack of 15°, the power input was observed to be always positive. This finding is similar to the case of the mean angle of attack of 0° in [40] (note that the flow does not remain attached during oscillations due to the leading-edge separation and vortex shedding, hence there are similarities in both cases). Therefore, plunging airfoil in stalled flow is unlikely to experience single degree of freedom flutter. Of course, flutter for the combined pitching and plunging remains a possibility.

F. Sudden Lift Loss

A second interesting feature of the variation of the time-averaged lift data shown in Figs. 11 and 12 is the sudden drop in lift at higher Strouhal numbers (in the mode-2 regime), resulting in a lift coefficient approximately equal to that of a stationary airfoil. No significant drop was observed for low amplitudes a/c = 0.025 and 0.050. It is clear from Figure 11 that the lift drop occurs at lower frequencies for larger amplitudes. The observed trend of increasing Strouhal number with decreasing amplitude again implies a possible dependence on Strouhal number based on amplitude. Shown in Fig. 15 is therefore time-averaged lift coefficient against Strouhal number based on amplitude. Figure 15 shows that the data for different amplitudes collapse onto an approximate linear trend until the occurrence of the drop in lift in the range $Sr_A = 0.45 \pm 0.05$. Hence the smaller amplitudes did not display the drop in lift as the maximum Sr_A was insufficient (0.30 for a/c = 0.050, and 0.15 for a/c = 0.025).

To understand the cause of the sudden lift loss, Fig. 16 shows a selection of phase-averaged vorticity contour plots for a/c = 0.15 representing points before the fall (a and b), at the peak (c), and after the fall (d). Figure 16(a) and (b) display behavior typical of a mode-1 flowfield, i.e., a leading-edge vortex forms during the downward motion and is convected into the wake where it interacts with the trailing-edge vortex, or in the case of (a), its interaction with the trailing-edge forms the trailing-edge vortex prematurely. On the other hand, Fig. 16(c) displays a typical mode-2 flowfield. It also shows the beginning of the formation of a lower surface leading-edge vortex (see Fig. 16(c) left). With the Strouhal number increased to Sr_A = 0.525 (Fig. 16(d)) the flowfield is again

representative of a mode-2 but with a much larger and stronger lower surface vortex. It is therefore the creation of the lower surface vortex, which produces a low pressure region on the lower surface of the airfoil, that is the principle reason for the fall in lift.

Fig. 17 shows the strength of these vortices quantified in the form of peak circulation. From the phase-averaged velocity measurements at eight phases in the cycle, the vortices were followed after their formation and the peak circulation was calculated. Figure 17 shows the upper surface vortex gradually increasing in strength with increasing Strouhal number. The lower surface vortex only becomes discernible once $Sr_A > 0.3$, but after this point increases in strength with a far steeper gradient. As a result it becomes nearly equal to the circulation of the upper surface vortex once $Sr_A > 0.50$ and may even exceed it at higher Strouhal numbers. Therefore, for the case of Fig. 16(d) ($Sr_A = 0.525$) the lower surface vortex has more or less the same peak circulation as that of the upper surface. The asymmetry in vortex strength is therefore absent which correlates well with a lift coefficient that is approximately equal to that of a stationary airfoil.

The underlying question is therefore why does the lower surface vortex increase in circulation at a greater rate than the upper surface vortex? The explanation is shown in the left plot of Fig. 16(d). At the trailing-edge there is pairing of the clockwise and counter-clockwise trailing-edge vortices. The resulting vortex dipole convects in a downwards direction creating a downward deflected jet. Similar cases, a downward deflected jet accompanying low lift, have previously been reported for smaller angles of attack [29]. In these cases the explanation for the low lift was that the downward deflected jet draws fluid from the lower surface and therefore acts to strengthen the lower

surface vortex. We believe that the deflected jet and resulting strong lower surface vortex are responsible for the lift loss.

V. Conclusions

PIV and force measurements show that small amplitude ($a/c \leq 0.2$) plunge oscillations of a NACA 0012 airfoil can significantly increase lift and reduce drag. At low Strouhal numbers phase-averaged PIV measurements show leading edge vortices form, and are convected into the wake where they interact with vortices shed from the trailing edge. These leading-edge vortices act to increase the momentum transfer between the free stream and separation region leading to reduced time-averaged separation. With increasing Strouhal number, the multiple leading-edge vortices form into a single stronger leading-edge vortex that is shed later in the cycle. This was termed a mode-1 flow field, which is associated with efficient high-lift generation and low-thrust production. The degree of lift enhancement was shown to have an approximately linear proportionality with plunge velocity. The largest recorded increase in lift was 310% over the value for a stationary airfoil.

Multiple local peaks were observed in the time-averaged lift for all amplitudes. Both Reynolds number and amplitude had a weak effect on the values of Strouhal numbers at which these peaks occur. The modified lift coefficient based on the vector sum of the freestream velocity and maximum plunge velocity clearly shows the existence of three optimal regions in the amplitude-Strouhal number domain. These regions are centered

around Sr_c = 0.5, 1.0, and 2.0, and correspond to an optimum plunge velocity of roughly half the free stream velocity. The spectra of the velocity fluctuations in the wake of the stationary airfoil suggest that Sr_c = 0.5, 1.0, and 2.0 correspond to the subharmonic, fundamental, and the first harmonic of the natural shedding frequency. These measurements combined with the cross-correlation of the two-point velocity measurements in the spanwise direction confirm that resonance with the natural wake instabilities leads to improved lift generation.

At a critical Strouhal number, the leading-edge vortex convection is not seen and the vortex remains near the leading-edge. This was termed a mode-2 flow field, where a strong vortex-airfoil interaction takes place. The mode-2 leading-edge vortex is generated during the downward motion of the airfoil, but impinges with the upward moving airfoil resulting in the loss of its coherency. This strong interaction between the airfoil and vortex was studied by means of high-fidelity computational simulations. Instantaneous vorticity shows how the three-dimensionality of the leading-edge vortex increases and results in the breakdown of the vortical structure. The mode-2 flow field is characterized by low-lift and high-thrust. It is suggested that the high-thrust production is facilitated by greater shedding of vorticity at the trailing-edge and no interference from the leading-edge vortices in this mode. A sudden loss of lift may also occur for larger amplitudes in mode-2. This is due to the generation of a strong lower surface vortex that is reinforced through a downward deflected jet at the trailing-edge.

Acknowledgments

The experimental work was sponsored by the Air Force Office of Scientific Research, Air Force Material Command, USAF under grant numbers FA8655-09-1-3007 and FA8655-10-1-3093, as well as the Engineering and Physical Sciences Research Council (EPSRC) Studentship, and the RCUK Academic Fellowship in Unmanned Air Vehicles. The computational work was supported in part by AFOSR under a task monitored by Dr. D. Smith, and by a grant of HPC time from the DoD HPC Shared Resource Center at AFRL.

References

[1] Mueller, T. J., and DeLaurier, J. D., "Aerodynamics of Small Vehicles," *Annual Review of Fluid Mechanics*, Vol. 35, 2003, pp. 89–111.

[2] Shyy, W., Berg, M., and Ljungqvist, D., "Flapping and flexible wings for biological and micro air vehicles," *Progress in Aerospace Sciences*, Vol. 35, No. 5, 1999, pp. 455-505.

[3] Gursul, I., "Vortex Flows on UAVs: Issues and Challenges," *The Aeronautical Journal*, Vol. 108, No. 1090, December 2004, pp. 597-610.

[4] Zaman, K.B.M.Q., McKinzie, D.J., and Rumsey, C.L., "A natural low-frequency oscillations of the flow over an aerofoil near stalling conditions," *Journal of Fluid Mechanics*, Vol. 202, 1989, pp. 403-442.

[5] Gresham, N.T., Wang, Z., and Gursul, I., "Self-Induced Roll Oscillations of Nonslender Wings," *AIAA Journal*, Aerospace Letter, Vol. 47**,** Issue: 3**,** March 2009, Pages: 481-483.

[6] Gresham, N.T., Wang, Z., and Gursul, I., "Low Reynolds Number Aerodynamics of Free-to-Roll Low Aspect Ratio Wings," *Experiments in Fluids*, vol. 49, Issue 1, 2010, pp. 11-25.

[7] Yaniktepe, B. and Rockwell, D., “Flow Structure on a Delta Wing of Low Sweep Angle,” *AIAA Journal*, Vol. 42, No. 3, March 2004, pp. 513-523.

[8] Vardaki, E., Wang, Z., and Gursul, I., “Flow Reattachment and Vortex Re-formation on Oscillating Low Aspect Ratio Wings,” *AIAA Journal*, Vol. 46, No. 6, June 2008, pp. 1453-1462.

[9] Taylor, G., Wang, Z., Vardaki, E., and Gursul, I., “Lift Enhancement over Flexible Nonslender Delta Wings,” *AIAA Journal*, Vol. 45, No. 12, December 2007, pp. 2979-2993.

[10] Seifert, A., Greenblatt, D. and Wygnanski, I.J., “Active Separation Control; an Overview of Reynolds and Mach Number Effects,” *Aerospace Science and Technology*, Vol. 8, 2004, pp. 569-582.

[11] Raju, R., Mittal, R., Cattafesta, L.N., “Dynamics of Airfoil Separation Control Using Zero-Net Mass-Flux Forcing,” *AIAA Journal*, Vol. 46, No. 12, December 2008, pp. 3103-3115.

[12] Wu, J.Z., Lu, X.Y., Denny, A.G., Fan, M. and Wu, J.M., "Post-stall flow control on an airfoil by local unsteady forcing," *Journal of Fluid Mechanics*, Vol. 371, 1998, pp. 21-58.

[13] Miranda, S., Vlachos, P.P., Telionis, D.P. and Zeiger, M.D., "Flow control of a sharp-edged airfoil," *AIAA Journal*, Vol. 43, No. 4, 2005, pp. 716-726.

[14] Glezer, A., Amitay, M., and Honohan, A.M., “Aspects of Low- and High-Frequency Actuation for Aerodynamic Flow Control,” *AIAA Journal*, Vol. 43, No. 7, July 2005, pp. 1501-1511.

[15] Cleaver, D.J., Wang, Z.J. and Gursul, I., "Delay of Stall by Small Amplitude Airfoil Oscillation at Low Reynolds Numbers," *47th AIAA Aerospace Sciences Meeting, Orlando*, AIAA 2009-392, Florida, 2009.

[16] Cleaver, D.J., Wang, Z.J. and Gursul, I., "Lift Enhancement on Oscillating Airfoils," *39th AIAA Fluid Dynamics Conference,* AIAA 2009-4028, San Antonio, Texas, 2009.

[17] Visbal, M.R., “High-Fidelity Simulation of Transitional Flows past a Plunging Airfoil”, AIAA-2009-391. See also, *AIAA Journal*, Vol. 47, No. 11, 2009, pp. 2685-2697.

[18] Heathcote, S., "Flexible Flapping Airfoil Propulsion at Low Reynolds Numbers," Ph.D. Dissertation, Dept of Mechanical Engineering, University of Bath, Bath, 2006.

[19] Moffat, R.J., "Using Uncertainty Analysis in the Planning of an Experiment," *Journal of Fluids Engineering - Transactions of the ASME*, Vol. 107, No. 2, 1985, pp. 173-178.

[20] Frampton, K.D., Goldfarb, M., Monopoli, D. and Cveticanin, D., "Passive aeroelastic tailoring for optimal flapping wings," *Proceedings of Conference on Fixed, Flapping and Rotary Wing Vehicles at Very Low Reynolds Numbers*, Notre Dame, USA, 2000, pp. 473-482.

[21] Graftieaux, L., Michard, M. and Grosjean, N., "Combining PIV, POD and vortex identification algorithms for the study of unsteady turbulent swirling flows," *Measurement Science & Technology*, Vol. 12, No. 9, 2001, pp. 1422-1429.

[22] Morgan, C.E., Babinsky, H. and Harvey, J.K., "Vortex Detection Methods for use with PIV and CFD data," *47th AIAA Aerospace Sciences Meeting*, AIAA-2009-74, Orlando, Florida, 2009.

[23] Godoy-Diana, R., Marais, C., Aider, J.L. and Wesfreid, J.E., "A model for the symmetry breaking of the reverse Benard-von Karman vortex street produced by a flapping foil," *Journal of Fluid Mechanics*, Vol. 622, 2009, pp. 23-32.

[24] Anderson, D.A., Tannehill, J.C. and Pletcher, R.H., *Computational Fluid Mechanics and Heat Transfer*, McGraw-Hill Book Company, 1984.

[25] Visbal, M.R. and Rizzetta, D.P., "Large-eddy simulation on curvilinear grids using compact differencing and filtering schemes," *Journal of Fluids Engineering - Transactions of the ASME*, Vol. 124, No. 4, 2002, pp. 836-847.

[26] Visbal, M.R., Morgan, P.E. and Rizzetta, D.P., "An Implicit LES Approach Based on High-Order Compact Differencing and Filtering Schemes," *16th AIAA Computational Fluid Dynamics Conference*, AIAA 2003-4098, Orlando, Florida, 2003.

[27] Visbal, M.R. and Gaitonde, D.V., "High-order-accurate methods for complex unsteady subsonic flows," *AIAA Journal*, Vol. 37, No. 10, 1999, pp. 1231-1239.

[28] Visbal, M.R. and Gaitonde, D.V., "On the Use of High-Order Finite-Difference Schemes on Curvilinear and Deforming Meshes," *Journal of Computational Physics*, Vol. 181, 2002, pp. 155-185.

[29] Cleaver, D.J., Gursul, I. and Wang, Z., "Vortex Mode Bifurcation and Lift Force of a Plunging Airfoil at Low Reynolds Numbers," *48th AIAA Aerospace Sciences Meeting, Orlando*, AIAA 2010-390, Florida, 2010.

[30] Sunada, S., Yasuda, T., Yasuda, K. and Kawachi, K., "Comparison of wing characteristics at an ultralow Reynolds number," *Journal of Aircraft*, Vol. 39, No. 2, 2002, pp. 331-338.

[31] Schluter, J.U., "Lift Enhancement at Low Reynolds Numbers using Pop-up Feathers," *39th AIAA Fluid Dynamics Conference*, AIAA 2009-4195, San Antonio, Texas, 2009.

[32] Lai, J.C.S. and Platzer, M.F., "Jet characteristics of a plunging airfoil," *AIAA Journal*, Vol. 37, No. 12, 1999, pp. 1529-1537.

[33] Young, J. and Lai, J.C.S., "Oscillation frequency and amplitude effects on the wake of a plunging airfoil," *AIAA Journal*, Vol. 42, No. 10, 2004, pp. 2042-2052.

[34] Platzer, M., Jones, K.D., Young, J., and Lai, J.C.S., "Flapping-Wing Aerodynamics: Progress and Challenges," *AIAA Journal*, Vol. 46, No. 9, September 2008, pp. 2136-2149.

[35] Andro, J.Y. and Jacquin, L., "Frequency effects on the aerodynamic mechanisms of a heaving airfoil in a forward flight configuration," *Aerospace Science and Technology*, Vol. 13, No. 1, 2009, pp. 71-80.

[36] Fage, A. and Johansen, F.C., "On the Flow of Air Behind an Inclined Flat Plate of Infinite Span," *Proceedings of the Royal Society of London Series A*, Vol. 116, 1927, pp. 170-197.

[37] Abernathy, F.H., "Flow Over an Inclined Plate," *Transactions of the ASME - Journal of Basic Engineering*, Vol. 84, 1962, pp. 380 - 388.

[38] Huang, R.F. and Lin, C.L., "Vortex Shedding and Shear-Layer Instability of Wing at Low-Reynolds Numbers," *AIAA Journal*, Vol. 33, No. 8, 1995, pp. 1398-1403.

[39] Bearman, P.W., "Vortex Shedding from Oscillating Bluff-Bodies," *Annual Review of Fluid Mechanics*,Vol. 16, 1984, pp. 195-222.

[40] Heathcote, S., Wang, Z. and Gursul, I., "Effect of Spanwise Flexibility on Flapping Wing Propulsion", *Journal of Fluids and Structures*, vol. 24, 2008, pp. 183-199.

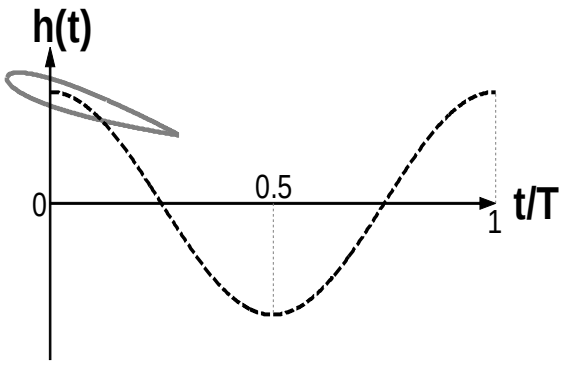

Fig. 1 Schematic of the plunging motion.

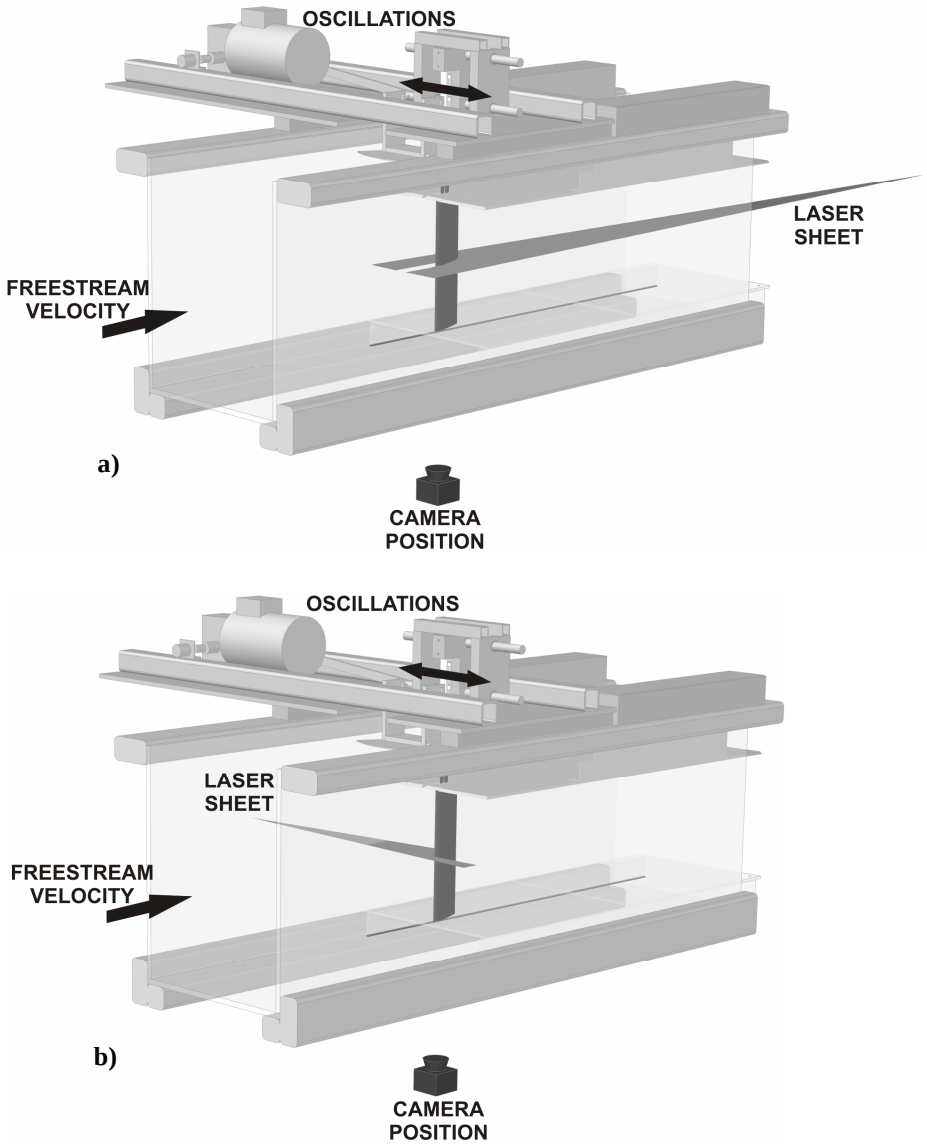

Fig. 2 Experimental setup a) for PIV measurements over the upper surface, and b) for PIV measurements over the lower surface.

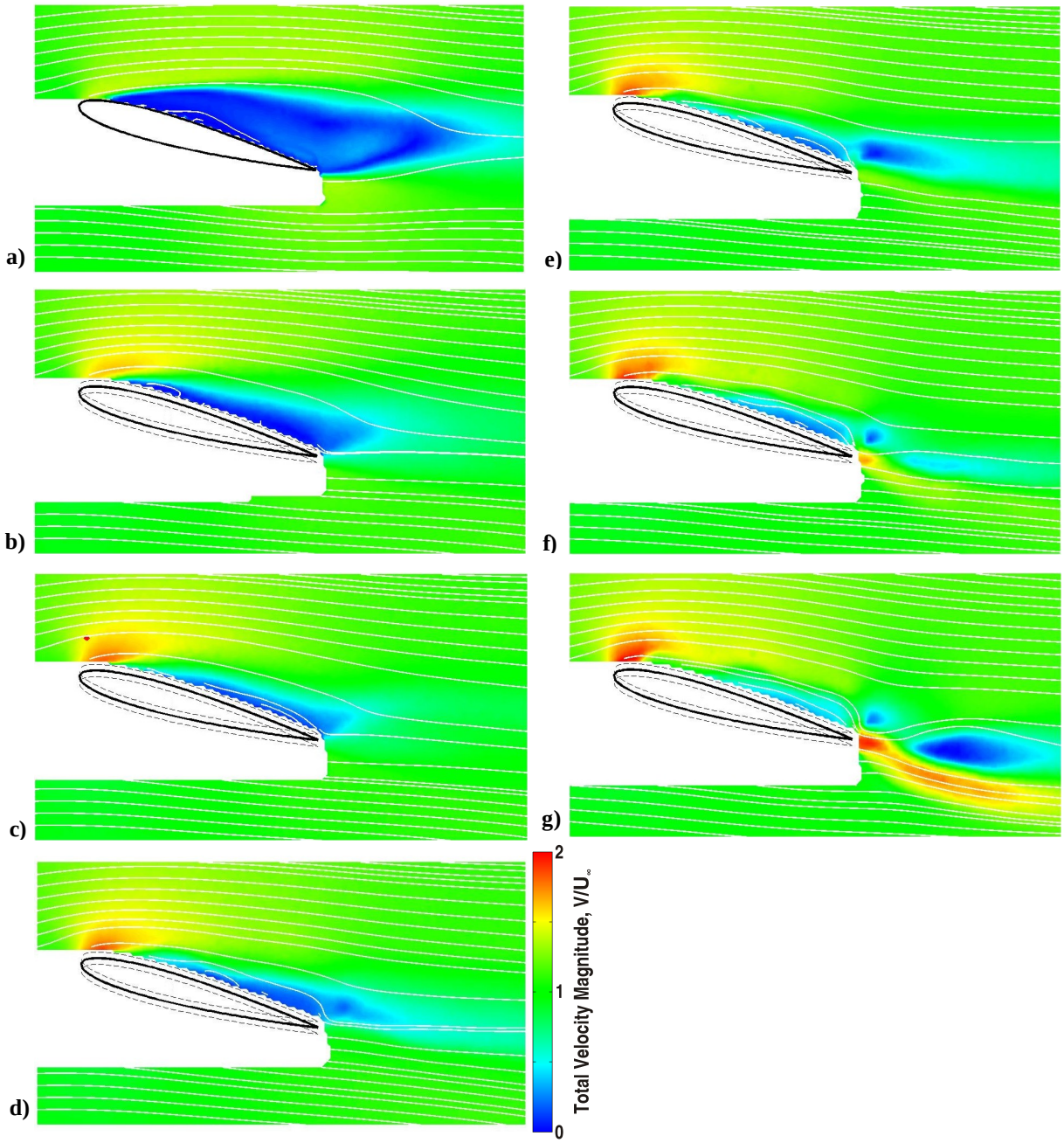

Fig. 3 Magnitude of measured time-averaged velocity for a/c = 0.025: a) stationary; b) Sr_c = 0.5; c) Sr_c = 1.0; d) Sr_c = 1.5; e) Sr_c = 2.0; f) Sr_c = 2.5 and g) Sr_c = 3.0.

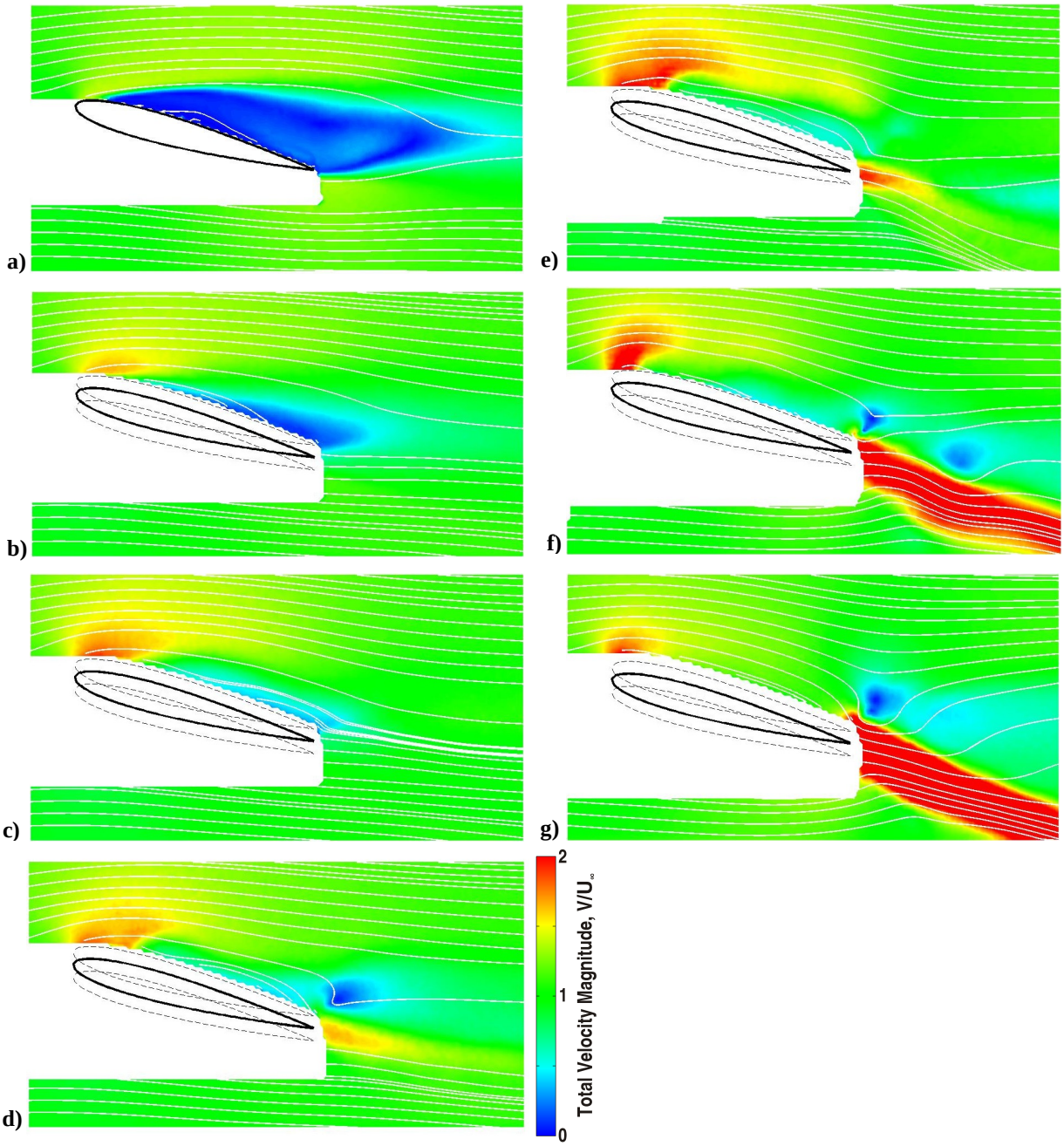

Fig. 4 Magnitude of measured time-averaged velocity for a/c = 0.050: a) stationary; b) Sr_c = 0.5; c) Sr_c = 1.0; d) Sr_c = 1.5; e) Sr_c = 2.0; f) Sr_c = 2.5 and g) Sr_c = 3.0.

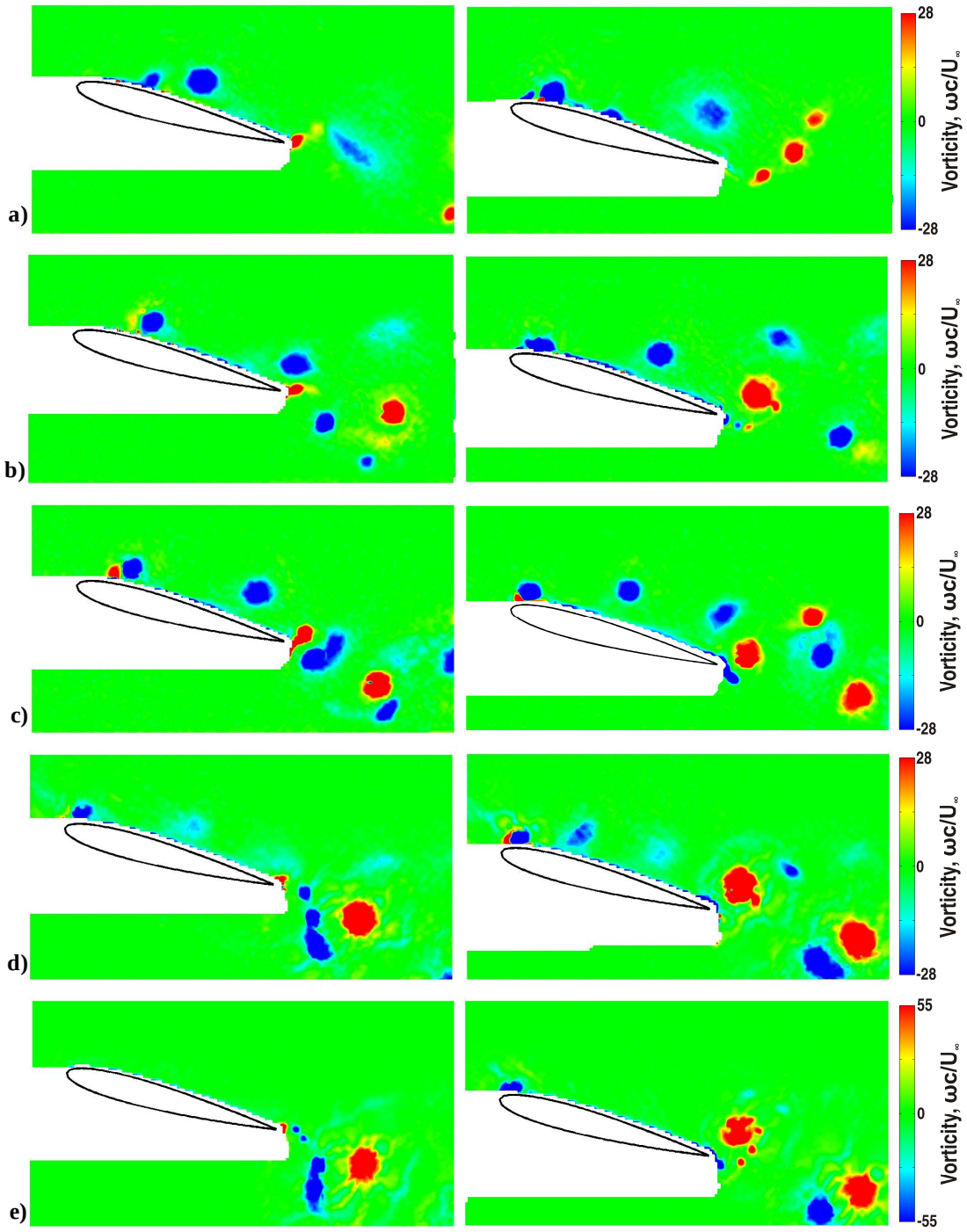

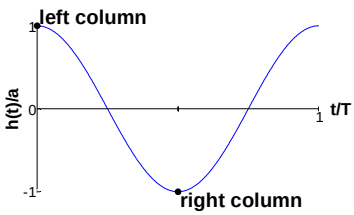

Fig. 5 Phase-averaged vorticity from PIV measurements at top (left) and bottom (right) of airfoil displacement for a/c = 0.050: a) Sr_c = 1.0; b) Sr_c = 1.5; c) Sr_c = 2.0; d) Sr_c = 2.5; e) Sr_c = 3.0. a) through c) demonstrate mode-1, e) demonstrates mode-2, and d) demonstrates a mixed mode. Note the different scale for e).

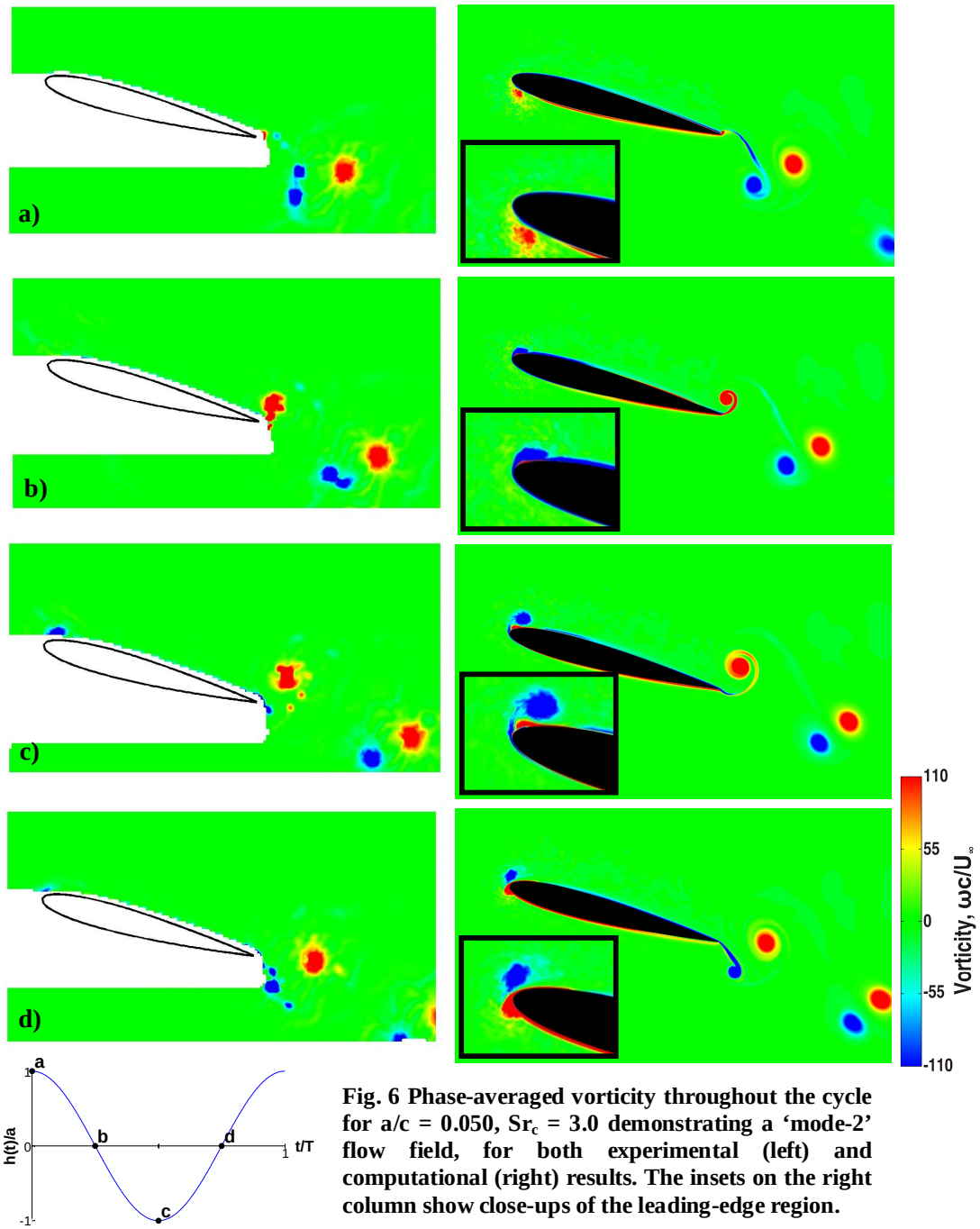

Fig. 6 Phase-averaged vorticity throughout the cycle for a/c = 0.050, Sr_c = 3.0 demonstrating a 'mode-2' flow field, for both experimental (left) and computational (right) results. The insets on the right column show close-ups of the leading-edge region.

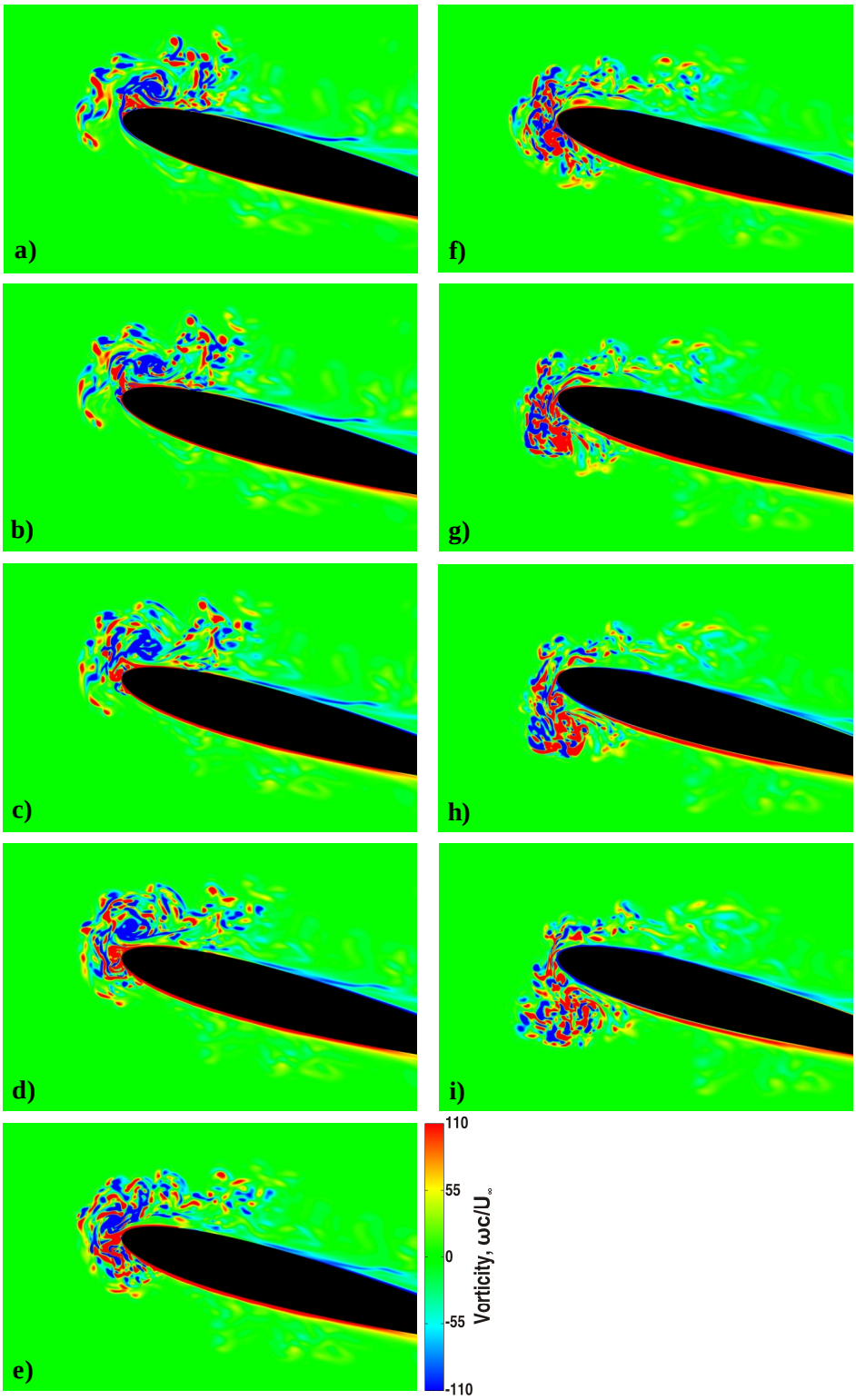

Fig. 7 Instantaneous vorticity contour plots from computational simulations for a/c = 0.050 Sr_c = 3. Moving upwards from bottom to top of the motion, exact position in the cycle denoted by diagram to left.

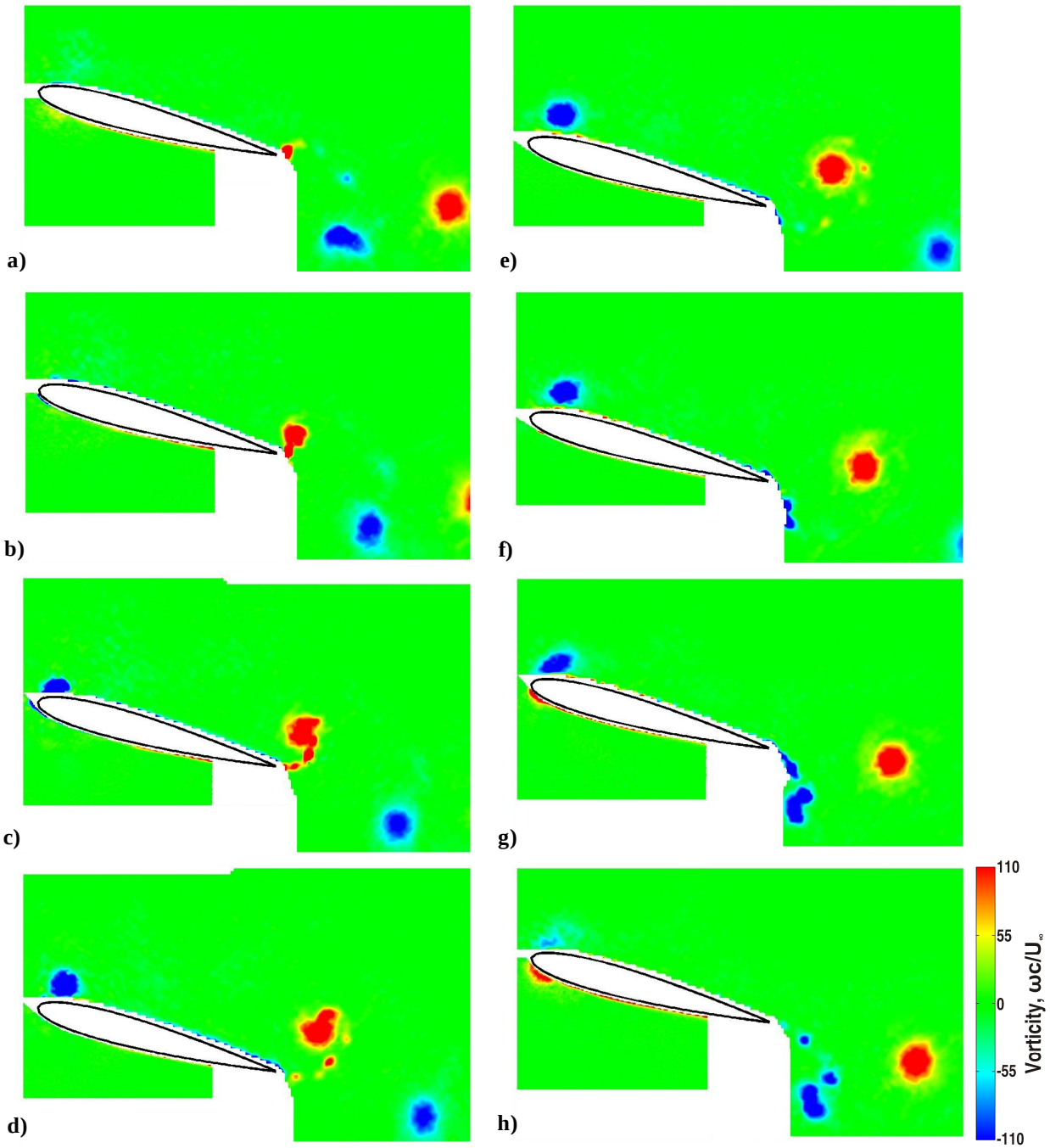

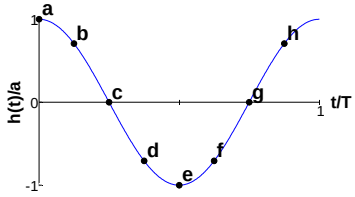

Fig. 8 Phase-averaged vorticity, $\omega c/U_\infty$, from PIV measurements for both the upper and lower surface of a mode-2 flow field: a/c = 0.10 and Sr_c = 1.75. Position in the cycle denoted by diagram to left.

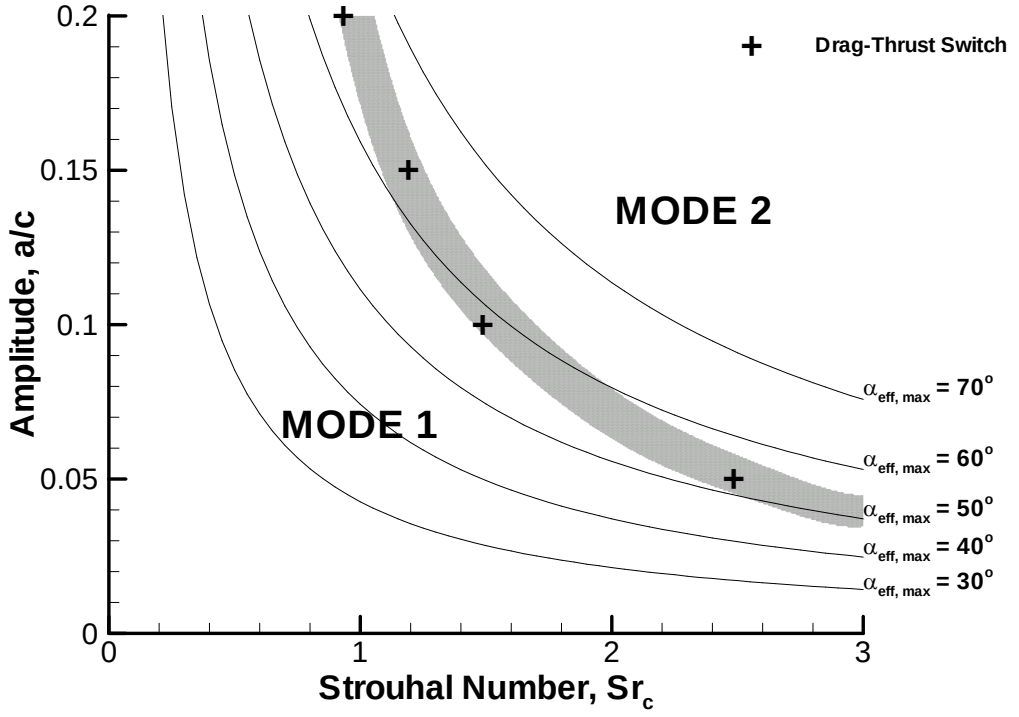

Fig. 9 Mode diagram derived from phase-averaged flow fields measured by PIV. The mode-switch boundary is represented by the shaded area.

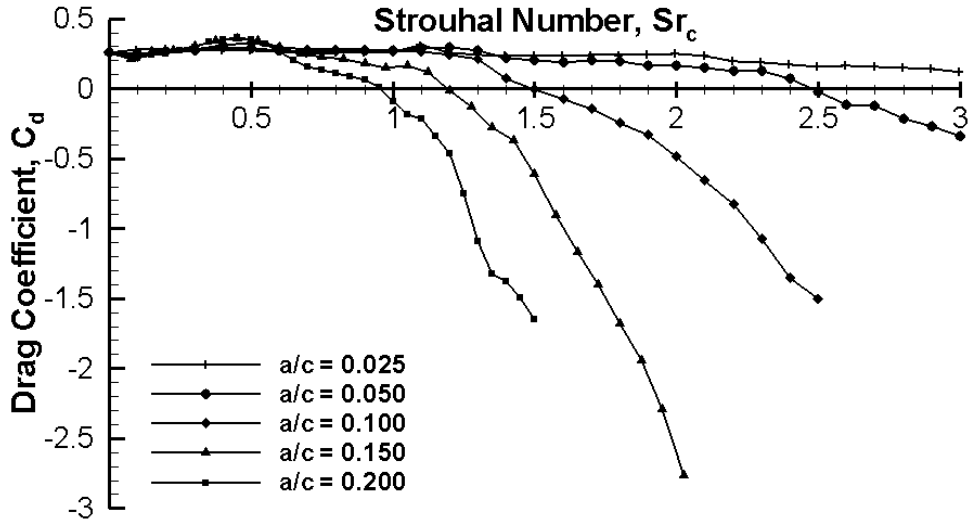

Fig. 10 Measured time-averaged drag coefficient for α = 15°, Re = 10, 000 and different amplitudes.

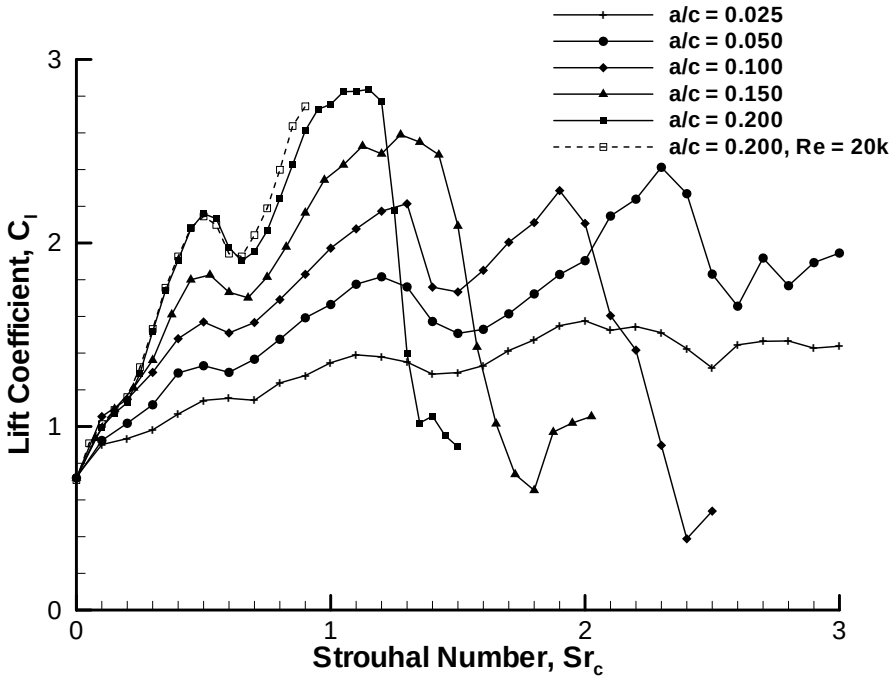

Fig. 11 Measured time-averaged lift coefficient for α = 15°, Re = 10, 000 and different amplitudes.

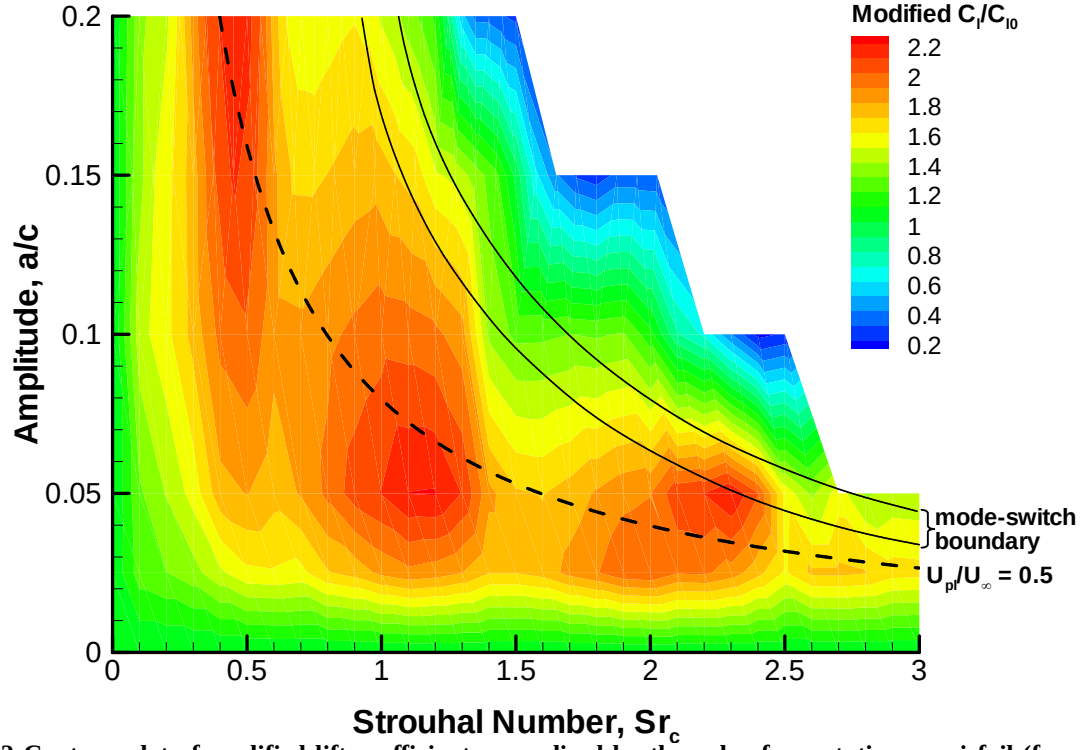

Fig. 12 Contour plot of modified lift coefficient normalized by the value for a stationary airfoil (from force measurements). Solid lines represent the mode-switch boundary from Fig. 9. Dashed line represents a constant normalized plunge velocity.

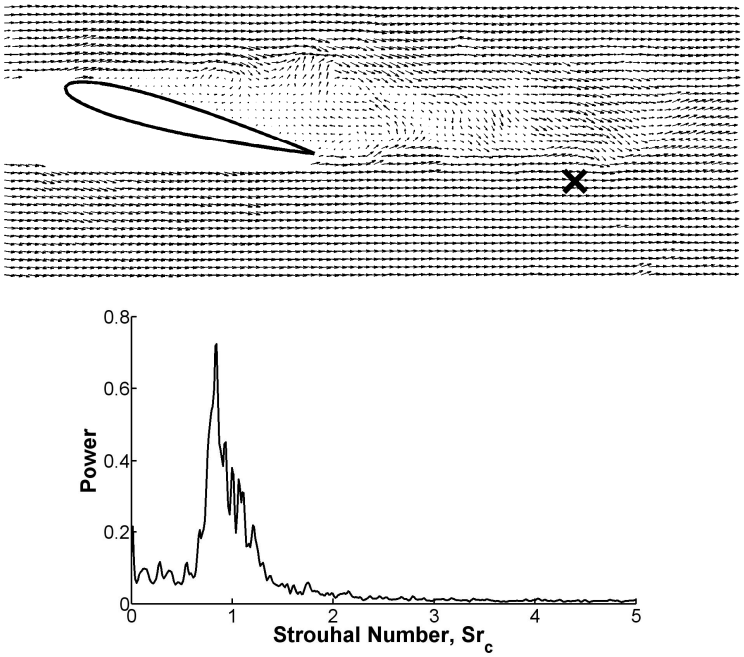

Fig. 13 Typical frequency spectra for a hot-film placed in the wake of the stationary airfoil. The position of the hot-film in the x-y plane is shown in the vector arrow plot above, in the z-plane it was positioned in the mid-span.

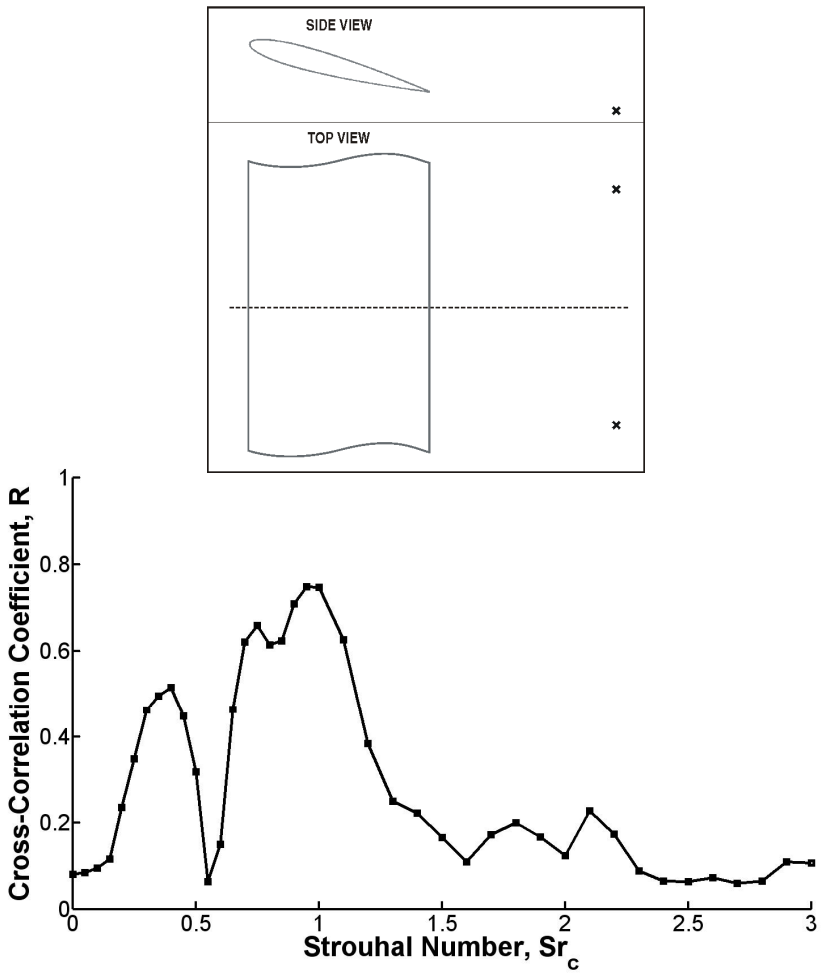

Fig. 14 Cross-correlation measurements in the wake of the plunging airfoil for a/c = 0.025. The two hot films were positioned in the x-y plane as shown above and separated in the z-plane symmetrically about the mid-span by 1.3c.

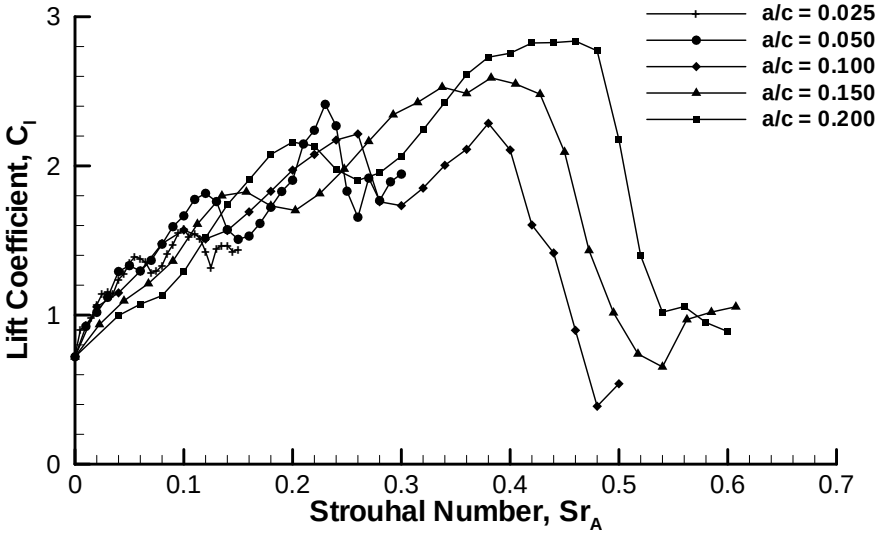

Fig. 15 Measured time-averaged lift coefficient for α = 15°, Re = 10, 000 and different amplitudes.

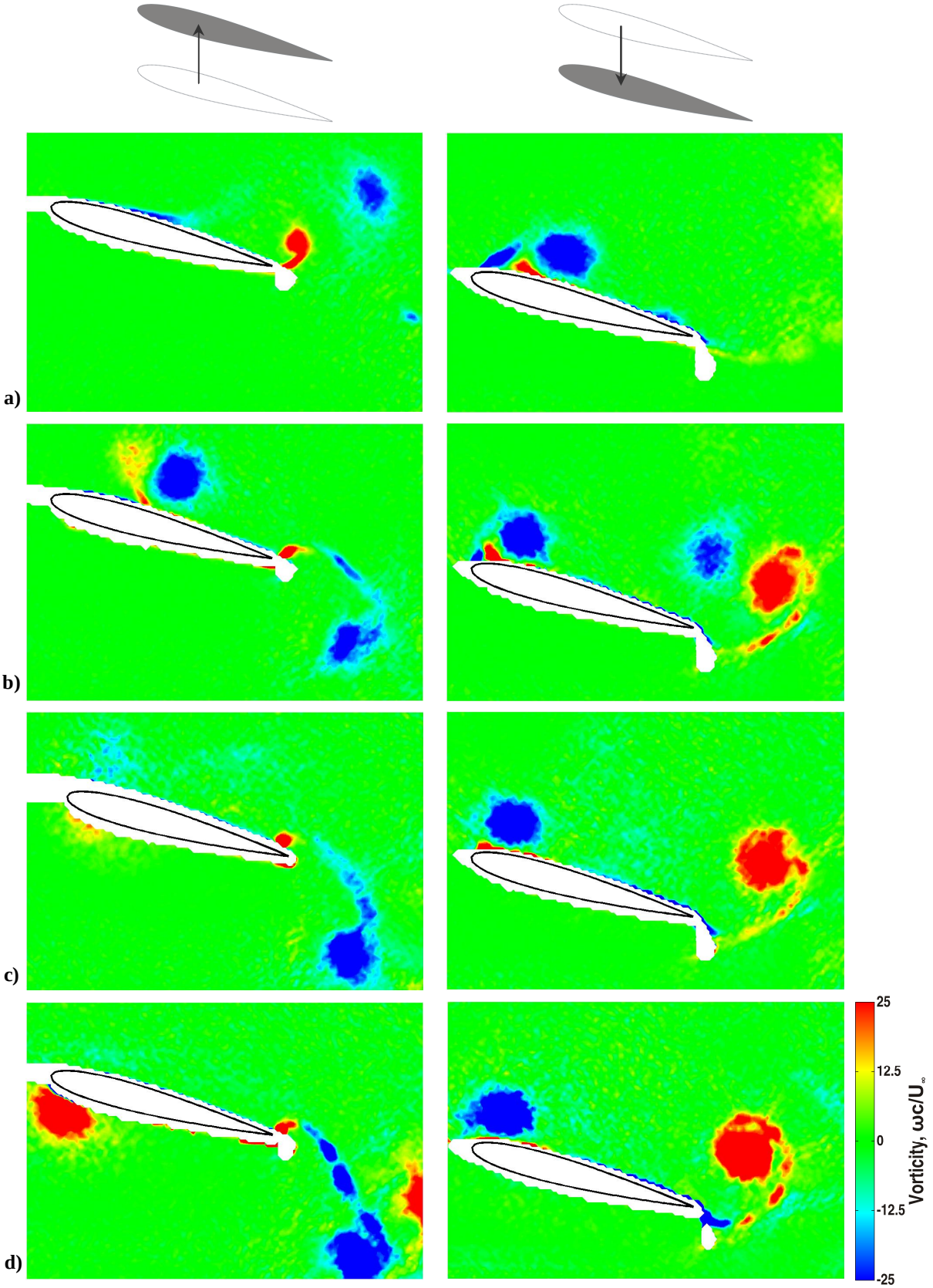

Fig. 16 Normalized vorticity from PIV measurements at top (left) and bottom (right) of motion with a/c = 0.15, α = 15°, Re = 10,000, for: a) Sr_A = 0.15 (Sr_c = 0.50), b) Sr_A = 0.30 (Sr_c = 1.00), c) Sr_A = 0.375 (Sr_c = 1.25), d) Sr_A = 0.525 (Sr_c = 1.75).

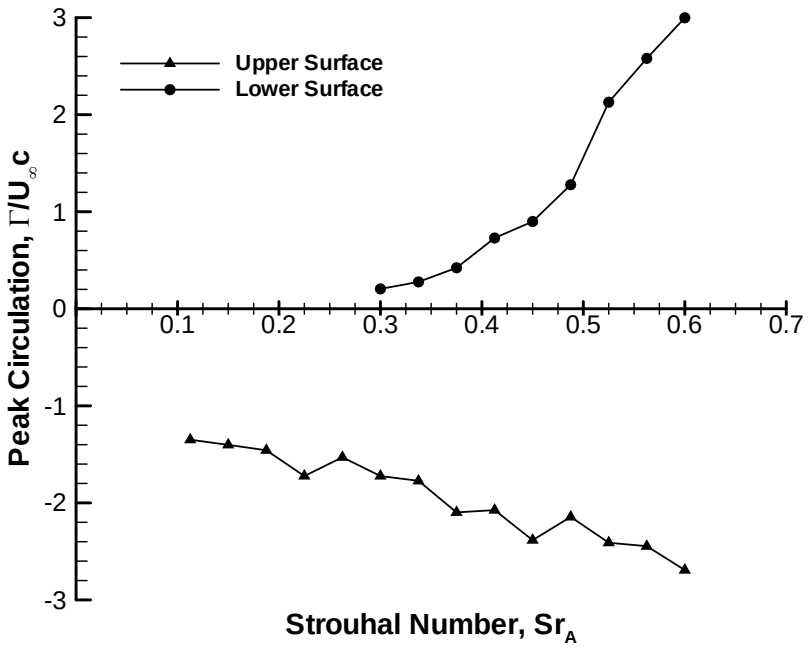

Fig. 17 Peak normalized LEV circulation for upper and lower surface for a/c = 0.15, calculated from PIV measurements.